ChemComm

Chemical Communications

Accepted Manuscript

ROYAL SOCIETY OF CHEMISTRY

rsc.li/chemcomm

COMMUNICATION

Perovskite chemical gardens: Highly fluorescent microtubes from self-assembly and ion exchange

Bruno C. Batista and Oliver Steinbock *

Received 00th January 20xx,
Accepted 00th January 20xx

DOI: 10.1039/x0xx00000x

We report the shape-preserving conversion of self-assembled $CaCO_3$ microtubes to $PbCO_3$ and $MAPbBr_3$ perovskite. The first step induces the growth of cerussite needles on the outer surface. When further converted, these hedgehog-like structures become fluorescent. Additional spatial control of the process yields Janus tubes of $CaCO_3$ and perovskite segments.

Self-assembly and self-organization are scientifically interesting and technologically promising processes that extend chemical complexity into the macroscopic world. They create multi-scale hierarchical order, result in novel functionalities, and can produce adaptive materials. It is therefore not surprising that living systems utilize these approaches to upgrade low-performance materials and to create macroscopic structures that do not follow from molecular symmetries. Examples include calcite-based sea shells[1a], light-harvesting architectures in silica sponges[1b], and chitin-bound goethite teeth of certain snails that are the strongest biological material[1c]. Chemists are only beginning to tap into the potential of self-assembly and self-organization, although man-made approaches promise additional rewards as emergent processes can be combined with rational design strategies.[2]

Chemical gardens are arguably the most iconic example of emergent abiotic structures.[3] These hollow tubes and shells form at the interface of two solutions capable of producing precipitates or other solids. In the classic form of the experiment, a metal salt seed is submerged in a sodium silicate solution and produces centimeter-scale structures consisting of metal hydroxide and silica; however, the shape-generating processes occur for numerous other reactions including those producing metal phosphates, sulfides, and borates as well as polyoxometalates and certain organic gels.[4] Among these diverse chemical garden systems, the growth of $CaCO_3$ microtubes on a specific type of ion exchange membrane (Nafion) is among the more poorly understood processes.[5] In these experiments, the membrane separates a $CaCl_2$ from a Na_2CO_3 solution, but allows for the slow permeation of calcium ions. After several days, small $CaCO_3$ tubes form on the Na_2CO_3 side of the membrane that often are conical and sometimes branched into T- or Y-shaped structures. Spectroscopic studies showed that the self-assembling tubes consist of either calcite or vaterite, two polymorphs of $CaCO_3$.

Here, we demonstrate the shape-conserving conversion of $CaCO_3$ tubes to $PbCO_3$ and subsequently to highly fluorescent perovskite structures. The latter class of materials has the general chemical formula ABX_3, where A can be a cation of methylammonium, B is usually Pb^{2+} or Sn^{2+}, and X is a halide ion.[6a] Furthermore, 3D perovskites have a cubic or pseudocubic (orthorhombic or tetragonal) crystal structure. They are semiconductors and attract considerable interest in the context of photovoltaics and other applications including uses as light emitting diodes, lasers, photodetectors, and catalysts.[6] Their synthesis can rely on different approaches ranging from solid-state (e.g. grinding) to hot-injection methods and ion replacement. The latter method has been pioneered by Yang et al. for nanomaterials both at solid-vapor and solid-liquid interfaces.[7] Noorduin et al. later demonstrated applications to $BaCO_3$-based microscale structures as well as biomineralized materials.[8] Our study is the first demonstration of shape-preserving perovskite production for chemical garden tubes. We also show that strong luminescence occurs already at relatively low conversion yields and that the yields can be greatly enhanced by long reaction times. The luminescent product tubes could find uses as flow-through sensors or catalysts in microfluidic applications[9] and self-propelled microtubes[10].

Figure 1 illustrates the steps of our synthesis protocol which begins with the self-assembly of hundreds of $CaCO_3$ microtubes on a Nafion 117 membrane. For these experiments, we 3D print a threaded connector joining two scintillation vials (Fig. 1a and Fig. S1, ESI). The cut membrane is placed between the vials and secured when the system is tightened. The lower vial holds a

Florida State University, Department of Chemistry and Biochemistry, Tallahassee, FL 32306-4390, USA. E-mail: osteinbock@fsu.edu
Electronic Supplementary Information (ESI) available: [details of any supplementary information available should be included here]. See DOI: 10.1039/x0xx00000x

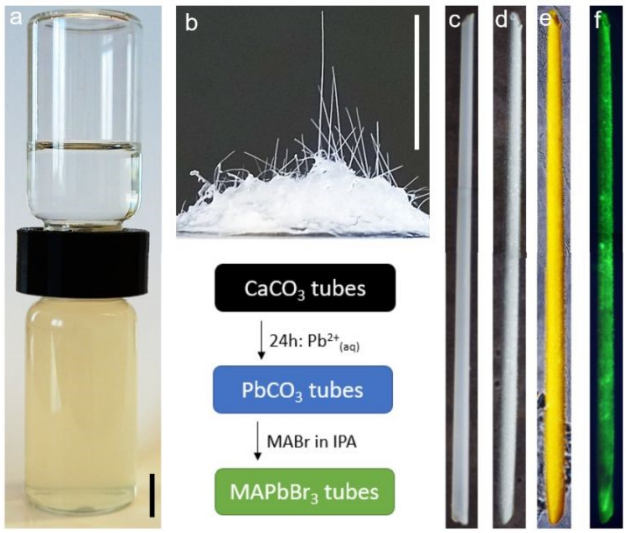

Fig. 1 (a) Experimental setup used to grow microtubes. (b) Microtubes and precipitates formed on a Nafion membrane. (c-d) Sequence of images showing successive conversion from (c) $CaCO_3$ to (d) $PbCO_3$ to perovskite under (e) white light and (f) 365 nm UV-light. Our naming convention for the different tubes does not imply pure substances. Scale bar: 1 cm. Length of tube in (c-f): 700 µm.

water-based agar gel (1% w/w) containing 1.0 M $CaCl_2$, while the upper one is filled with a 1.0 M Na_2CO_3(aq) solution. After one week, the membrane (Fig. 1b) is extracted, rinsed, and exfoliated. Earlier studies showed that these tubes (c) consist of either vaterite or calcite.[5, 10b] In our experiments, they have radii of 50 to 200 µm, lengths of up to several millimeters, and a wall thickness of 5 to 10 µm. The tubes are then transferred to an aqueous 10 mM lead acetate solution. After 1 day, we extract and rinse the tubes and dry the samples at 22 ˚C under N_2 gas. The resulting white lead tubes (d) are then exposed to a small amount of methylammonium bromide (MABr) dissolved in isopropyl alcohol (IPA) and, within seconds, turn yellow (e). The product tubes are brightly fluorescent under UV light emitting green light (f) as expected for the perovskite $MAPbBr_3$. Notice that the frames (c-f) show the same tube.

In the following, we characterize the microtube material at different stages of its preparation. Figures 2a,b show representative scanning electron microscopy (SEM) images of a tube before and after exposure to the lead acetate solution. The original $CaCO_3$ tube (a) has an overall smooth outer wall surface that only under close inspection reveals a slightly granular texture. The morphology of the white lead tube (b) is strikingly different as the surface has become decorated with densely packed needle-shaped crystals. This hedgehog-like appearance develops over the first 1-10 min of solution exposure and commences with the growth of hexagonal plate-like crystals that quickly cover the surface (Fig. S2, ESI) and in some samples show tight alignment (Fig. S3, ESI). Figure 2c shows a sequence of 12 optical micrographs illustrating that the needle-shaped crystals indeed form during the Pb^{2+}(aq) exposure and not during drying (see also movie S1, ESI). The observed surface textures are unique for chemical gardens and demonstrate that their microscale structure can be altered drastically by chemical processes and surface-bound crystal growth without loss of the main tubular shape.

Powder X-ray diffraction (XRD) patterns of the materials confirm that the initial tubes consist of the expected $CaCO_3$ and match the XRD patterns of the metastable polymorph vaterite and the stable polymorph calcite (Fig. 2d). The corresponding peaks are partially labeled as “V” and “C” for vaterite and calcite, respectively. For a sample comprised of hundreds of tubes, the (semi-quantitative) vaterite-to-calcite ratio is found as 76:24. Accordingly, vaterite is the dominant constituent.

After 24 h of exposure to the lead acetate solution, the XRD pattern indicates the presence of cerussite ($PbCO_3$) and hydrocerussite ($Pb_3(CO_3)_2(OH)_2$) (Fig. 2e). The corresponding major peaks are labeled as “Ce” and “H”, respectively. Based on our XRD result and the known crystal habits for these compounds[11,12], we assign the hexagonal plate-like crystals to hydrocerussite and the needle-like crystals in the late samples to cerussite. A whole pattern profile fitting of the XRD data also indicate the following (semi-quantitative) composition: 48% cerussite, 6% hydrocerussite, 24% vaterite, and 22% calcite. Raman spectroscopy suggests that the surface is completely converted to $PbCO_3$. The interior, however, remains mainly vaterite. Additional factors favoring the vaterite conversion could include sample porosities and crystallite sizes.

Figure 3a shows SEM images of a MABr-exposed tube. The overall appearance is similar to the intermediate structure in Fig. 2b, but the needle-like crystals on the outer surface are now more rounded. The micrograph in Fig. 3a is complemented by maps of the spatial distributions of Pb and Br. The maps are obtained by energy dispersive X-ray spectroscopy (EDS) which primarily probes a thin surface layer of the samples (< 1 µm). The outer surface shows high concentration of Pb while the corresponding Ca levels are essentially zero. The distribution of Br, indicative of successful production of the perovskite, overall

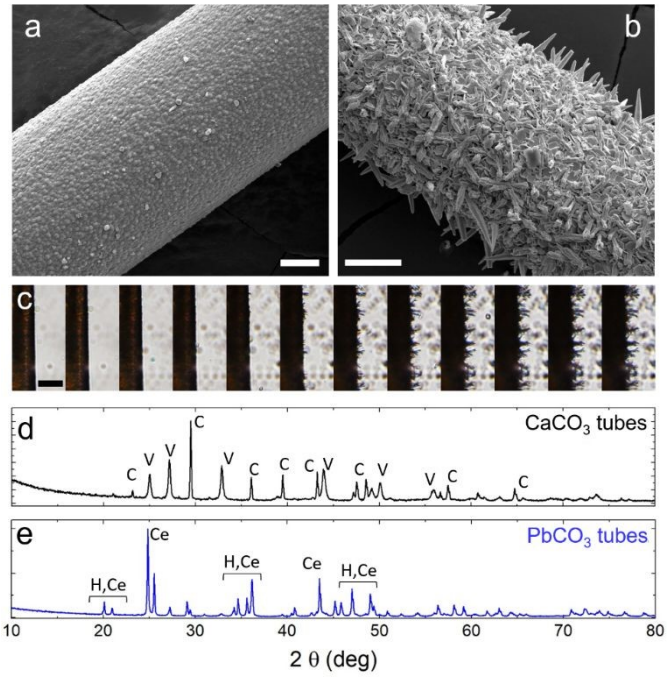

Fig. 2 Scanning electron micrographs of (a) $CaCO_3$ and (b) Pb-converted microtubes. (c) Twelve optical micrographs depicting needle growth over the course of 90 s. (d,e) X-ray diffraction pattern of microtubes. Scale bars are 20 µm.

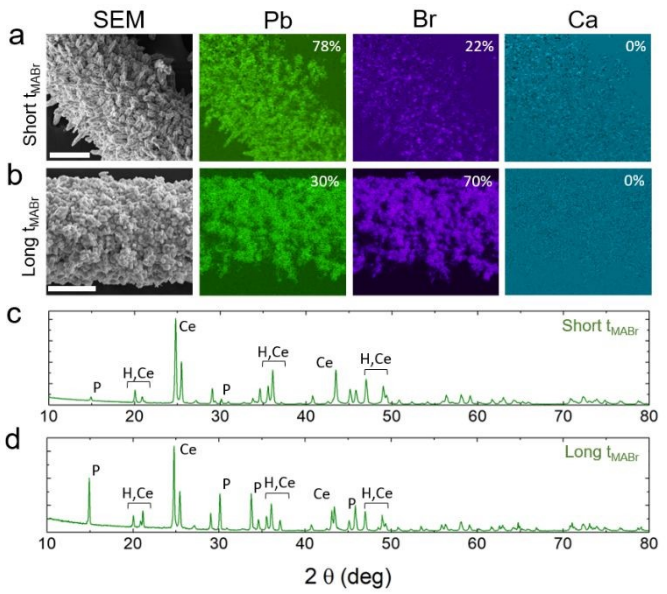

Fig. 3 Analysis of perovskite tubes obtained for short and long exposure times. (a,b) SEM images and EDS maps of Pb, Br, and Ca with average atomic percentages. (c,d) Corresponding XRD patterns. The specific conversion times are: (a,c) 24 h in Pb^{2+} followed by 1 min in MABr and (b,d) 35 d in Pb^{2+} followed by 12 h in MABr. Scale bars: 25 µm.

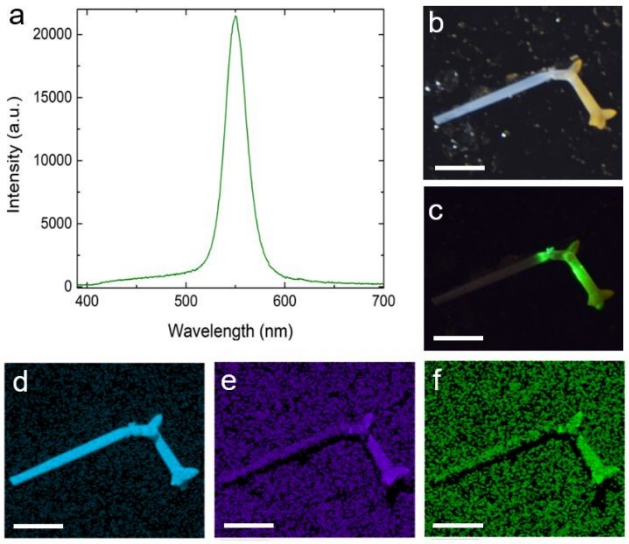

Fig. 4 (a) Photoluminescence spectrum of perovskite tubes. (b,c) Photographs of a Janus tube obtained by partial conversion of a vaterite tube under (b) white light and (c) UV illumination. (d-f) EDS maps of (d) Ca, (e) Br, and (f) Pb. Scale bars: 500 µm.

matches the one for Pb, but is more patchy, possibly due to the complex shapes of the surface-decorating crystals. Direct evidence for the production of $MAPbBr_3$ is given by the XRD data in Fig. 3c (see also Fig. S4, ESI) where two characteristic peaks are labeled as "P". The atomic percentages of Pb and Br are estimated to be 78% and 22%, respectively, suggesting a perovskite conversion factor of 7.3%. This yield is sufficient to convert the non-fluorescent reactant structures to highly luminescent tubes (see e.g. Fig. 1f).

To obtain insights into the bulk composition of the MABr-exposed tubes, we performed inductively coupled plasma mass spectrometry (Fig. S5, ESI) for which a large number of converted tubes were digested in nitric acid. Disregarding other elements, these experiments yield the following atomic percentages: 90% Pb and 10% Br. These percentages indicate a conversion factor to perovskite of 3.3%. The signal for Ca was near 0 and its relevance minimized due to signal interference from Ar. Additional evidence for the conversion of the outer surface is given by micro-Raman spectra (Fig. S6, ESI).

Higher conversion yields can be achieved by even longer exposure times and such experiments continue to preserve the tubular macroscopic shapes. For instance, we exposed the $CaCO_3$ tubes to Pb^{2+} for 35 days followed by 12 h in an IPA solution of MABr. Figure 3b shows SEM and EDS maps of a representative sample. The decrease in the percentage of lead accompanied by an increase in the amount of bromine indicates a much greater degree of surface conversion to perovskite (80%). This higher yield is also reflected in the XRD pattern (Fig. 3d) that shows a prominent peak at 15° which is indicative of perovskite. A whole pattern profile fitting with Rietveld refinement assigns 40% to $MAPbBr_3$, 43% to cerussite, and the remaining percentage mostly to vaterite and calcite. We note that EDS maps of the interior wall surface sometimes reveal notable Ca signals, indicating that part of the tube interior can remain unconverted.

The difference between the more deeply penetrating conversion to (hydro)cerussite and the—by comparison—surface-bound conversion to perovskite suggest different mechanisms. Earlier studies of calcite particles exposed to Pb^{2+}(aq) ions revealed the development of ~100 nm wide pores between calcite and the forming cerussite.[12] These gaps might boost dissolution via possible incursion of solution and explain that the replacement process penetrates the structures deeper than one might expect for a purely surface mediated process.

In the following, we analyze the photophysical features of tubes produced via our 24 h procedure (see Fig. 3a,c). Figure 4 shows the emission spectrum of a perovskite tube for an excitation wavelength of 365 nm. The emission signal is centered around 549 nm (green light) and has a half width at half maximum of 26 nm. Corresponding transient absorption measurements (Fig. S8) reveal a lifetime of 6.0 ns. These characteristics are in good agreement with earlier measurements of micrometer-scale $MAPbBr_3$ crystals.[8]

Lastly, we demonstrate that the conversion of vaterite tubes to perovskite can be performed locally to create Janus-like tubes. The process is based on the partial immersion of the sample into the reagent solutions. A representative example is shown in Figs. 4b-f in terms of optical micrographs obtained under white (b) and UV light (f) as well as EDS maps of Ca, Br, and Pb (d-f). For this branched tube only the shorter arm was converted while its longer branched remained $CaCO_3$ (see Fig. S9, ESI for additional examples).

In conclusion, we have converted self-assembled $CaCO_3$ microtubes to $PbCO_3$ and fluorescent $MAPbBr_3$ bearing structures while preserving the tubular shapes of the original structures. The first conversion step resulted in the growth of long needle-like cerussite crystals that decorate the originally smooth surface in a surprising fashion and constitute the first

example of such expansive crystal growth on chemical gardens. The second conversion step widely maintains this texture and results in green fluorescent microtubes. We suggest that these product tubes could find applications as sensors or catalytic segments in microfluidic devices and related applications.

This material is based upon work supported by NASA under grant no. 80NSSC18K1361. We thank Prof. Biwu Ma for help with reagents and Dr. Qingpu Wang for earlier experiments on $CaCO_3$ tube growth. We thank Dr. Xinsong Lin for assistance with XRD assignments, Dr. J. S. Raaj Vellore Winfred for helping with photoluminescence experiments and Dr. Eric Lochner for access and assistance with SEM/EDS analyses. We acknowledge the Condensed Matter and Material Physics User Facility and the X-Ray Crystallography Facility at Florida State University for access to instrumentation.

Notes and references

1 (*a*) J. Sun and B. Bhushan, *RSC Adv.*, 2012, **2**, 7616; (*b*) V. C. Sundar, A. D. Yablon, J. L. Grazul, M. Ilan and J. Aizenberg, *Nature*, 2003, **424**, 899; (*c*) A. H. Barber, D. Lu and N. M. Pugno, *J. R. Soc. Interface*, 2015, **12**, 20141326.

2 E. Nakouzi and O. Steinbock, *Sci. Adv.*, 2016, **2**, e1601144;

3 (*a*) L. M. Barge et al., *Chem. Rev.*, 2015, **115**, 8652; (*b*) O. Steinbock, J. H. E. Cartwright and L. M. Barge, *Physics Today*, 2016, **69**, 44.

4 (*a*) B. C. Batista and O. Steinbock, *Chem. Commun.*, 2015, **51**, 12962; (*b*) M. Emmanuel, E. Lantos, D. Horváth and Á. Tóth, *Soft Matter*, 2022, **18**, 1731; (*c*) A. G. Boulay, G. J. T. Cooper and L. Cronin, *Chem. Commun.*, 2012, **48**, 5088; (*d*) P. Kumar, C. Hajdu, Á. Tóth and D. Horváth, *ChemPhysChem*, 2021, **22**, 488; (*e*) E. A. B. Hughes, O. Jones-Salkey, P. Forey, M. Chipara and L. M. Grover, *ChemSystemsChem*, *2021*, **3**, e2000062; (*f*) P. J. Fryfogle, E. J. Nelson and J. J. Pagano, *Colloids and Surfaces A: Physicochem. Eng. Aspects*, 2015, **485**, 84; (*g*) M. H. Kumar, N. Yantara, S. Dharani, M. Graetzel, S. Mhaisalkar, P. P. Boix and N. Mathews, *Chem. Commun.*, 2013, **49**, 11089.

5 (*a*) M. Takiguchi, K. Igarashi, M. Azuma and H. Ooshima, *Cryst. Growth Des.*, 2006, **6**, 1611; (*b*) K. Igarashi, M. Takiguchi and H. Ooshima, *J. Ceram. Soc. Jpn.*, 2008, **116**, 111; (*c*) Y. Zhang, Y. Liu, X. Ji, C. E. Banks and W. Zhang, *Chem. Commun.*, 2011, **47**, 4126; (*d*) M. Getenet, J. Rieder, M. Kellermeier, W. Kunz and J. M. García-Ruiz, *Chem. Eur. J.*, 2021, **27**, 16135; (*e*) S. S. S. Cardoso, J. H. E. Cartwright, A. G. Checa and C. I. Sainz-Díaz, *Acta Biomaterialia*, 2016, **43**, 338; (*f*) S. S. S. Cardoso, J. H. E. Cartwright and C. I. Sainz-Díaz, *Icarus*, 2019, **319**, 337; (*g*) F. C. Donnelly, F. Purcell-Milton, V. Framont, O. Cleary, P. W. Dunne and Y. K. Gun'ko, *Chem. Commun.,* 2017, **53**, 6657; (*h*) X. Zhou, W. Liu, J. Zhang, C. Wu, X. Ou, C. Tian, Z. Lin and Z. Dang, *ACS Appl. Mater. Interfaces*, 2017, **9**, 35785.

6 (*a*) M. Worku, A. Ben-Akacha, T. B. Shonde, H. Liu and B. Ma, *Small Sci.*, 2021, **1**, 2000072; (*b*) X. Xu and X. Wang, *Small Structures*, 2020, **1**, 2000009; (*c*) J, J. Yoo, G. Seo, M. R. Chua, T. G. Park, Y. Lu, F. Rotermund, Y.-K. Kim, C. S. Moon, N. J. Jeon, J.-P. Correa-Baena, V. Bulović, S. S. Shin, M. G. Bawendi and J. Seo, *Nature*, 2021, **590**, 587; (*d*) J. Hwang, R. R. Rao, L. Giordano, Y. Katayama, Y. Yu and Y. Shao-Horn, *Science*, 2017, **358**, 751; (*e*) Q. He, M. Worku, H. Liu, E. Lochner, A. J. Robb, S. Lteif, J. S. R. V. Winfred, K. Hanson, J. B. Schlenoff, B. J. Kim and B. Ma, *Angew. Chem. Int. Ed.*, 2021, **60**, 2485; (*f*) S. Wang, L. Du, Z. Jin, Y. Xin and H. Mattoussi, *J. Am. Chem. Soc.*, 2020, **142**, 12669.

7 L. Dou, M. Lai, C. S. Kley, Y. Yang, C. G. Bischak, D. Zhang, S. W. Eaton, N. S. Ginsberg and P. Yang, *Proc. Natl. Acad. Sci. USA*, 2017, **140**, 7216.

8 (*a*) T. Holtus, L. Helmbrecht, H. C. Hendrikse, I. Baglai, S. Meuret, G. W. P. Adhyaksa, E. C. Garnett and W. L. Noorduin, *Nature Chem.*, 2018, **10**, 740; (*b*) L. Helmbrecht, M. H. Futscher, L. A. Muscarella, B. Ehrler and W. L. Noorduin, *Adv. Mater.*, 2021, **33**, 2005291; (*c*) G. Grimaldi, L. S. D. Antony, L. Helmbrecht, A. van der Weijden, S. W. van Dongen, I. Schuringa, J. Borchert, E. Alarcón-Lladó, W. L. Noorduin and B. Ehrler, *Appl. Phys. Lett.*, 2021, **119**, 223102; (*d*) A. van der Weijden, M. van Hecke and W. L. Noorduin, *Cryst. Growth Des.*, 2022, **22**, 2289.

9 (*a*) Q. Wang and O. Steinbock, *ChemCatChem*, 2020, **12**, 63; (*b*) Q. Wang, E. Nakouzi, E. A. Ryan and C. V. Subban, *Environ. Sci. Technol. Lett.* 2022, **9**, 645.

10 (*a*) Q. Wang, P. Knoll and O. Steinbock, *J. Phys. Chem. B*, 2021, **125**, 13908; (*b*) Q. Wang and O. Steinbock, *Phys. Chem. Chem. Phys.,* 2022, **24**, 14538.

11 (*a*) M. H. Brooker, S. Sunder, P. Taylor and V. J. Lopata, *Can. J. Chem*., 1983, **61**, 494; (*b*) K. Wang, L. Li, M. Shellaiah and K. W. Sun, *Sci. Rep.*, 2017, **7**, 13643.

12 (*a*) A. A. Rouff, E. J. Elzinga, R. J. Reeder and N. S. Fisher, *Environ. Sci. Technol.*, 2006, 40, 1792; (*b*) K. Yuan, S. S. Lee, V. De Andrade, N. C. Sturchio and P. Fenter, *Environ. Sci. Technol.*, 2016, **50**, 12984; (*c*) B. Abdilla, D. J. Minahan, J. P. Gleghorn, Y. Kim, S. S. Lee, P. Fenter and N. C. Sturchio, *ACS Earth Space Chem.,* 2022, **6**, 861; (*d*) X. Zhou, W. Liu, J. Zhang, C. Wu, X. Ou, C. Tian, Z. Lin and Z. Dang, *ACS Appl. Mater. Interfaces*, 2017, **9**, 35785.